



Effect of austempering temperature on microstructure and cyclic deformation behaviour of multiphase low-carbon steel

X. Y. Long^{1,2} · R. Branco³ · W. Macek⁴ · R. Masoudi Nejad⁵ · G. Lesiuk⁶ · S. P. Zhu⁷ · A. M. Amaro³

Received: 3 March 2023 / Revised: 23 June 2023 / Accepted: 29 June 2023 / Published online: 14 July 2023
© The Author(s) 2023

Abstract

This paper examined the cyclic deformation behaviour of multiphase low-carbon steel that was subjected to austempering heat treatments at four temperatures (190 °C, 230 °C, 275 °C, and 315 °C) below the martensite start temperature ($M_s = 353$ °C). The tests were conducted at room temperature, under fully reversed strain-controlled conditions, with strain amplitudes in the range 0.5–1.0%. The microstructure was observed by transmission electron microscopy, and the fracture surfaces were examined by scanning electron microscopy. The steel had a bainite/martensite microstructure, with increasing bainite content for higher austempering temperatures. Irrespective of the tested conditions, it strain-hardened during the first two cycles and then, strain-softened until failure. The austempering temperature did not significantly affect the stress-based, strain-based and energy-based relationships. However, lower austempering temperatures slightly improved the fatigue performance.

Keywords Low-carbon steel · Austempering temperature · Low-cycle fatigue · Fatigue behaviour

List of symbols

b Fatigue strength exponent
 c Fatigue ductility exponent
 c_i Fitting constants
 D_1, D_2 Degree of strain hardening
 D_3 Degree of strain softening

$d\epsilon/dt$ Strain rate
 E Young's modulus
 K' Cyclic strain-hardening coefficient
 n' Cyclic strain-hardening exponent
 M_s Martensite transformation temperature
 N_f Number of cycles to failure
 R^2 Coefficient of correlation
 R_ϵ Strain ratio
 T Austempering temperature
 T_{opt} Optimum austempering temperature
 V_B Volume fraction of bainite
 V_M Volume fraction of martensite
 V_{RA} Volume fraction of retained austenite
 ΔW_0^+ Tensile elastic energy at the material fatigue limit
 ΔW_p Plastic strain energy density of the half-life cycle
 ΔW_T Total strain energy density of the half-life cycle
 ϵ_a Strain amplitude of the half-life cycle
 ϵ'_f Fatigue ductility coefficient
 $\sigma_{a,1}$ Stress amplitude of the first cycle
 σ_a Stress amplitude of the half-life cycle
 $\sigma_{a,max}$ Maximum value of stress amplitude
 σ_a Stress amplitude of the half-life cycle
 σ'_f Fatigue strength coefficient
 σ_{max} Maximum tensile stress of the half-life cycle
 α_p Coefficient of the plastic strain energy versus life curve

✉ W. Macek
wojciech.macek@pg.edu.pl

¹ State Key Laboratory of Metastable Materials Science and Technology, Yanshan University, Qinhuangdao 066004, China

² Guangzhou University of Navigation, Guangzhou 510725, Guangdong, China

³ Department of Mechanical Engineering, CEMMPRE, University of Coimbra, Rua Luis Reis Santos, 3030-788 Coimbra, Portugal

⁴ Faculty of Mechanical Engineering and Ship Technology, Gdansk University of Technology, 11/12 Gabriela Narutowicza, 80-233 Gdansk, Poland

⁵ Faculty of Human Settlements and Civil Engineering, Xi'an Jiaotong University, Xi'an, China

⁶ Faculty of Mechanical Engineering, Wrocław University of Science and Technology, Wrocław, Poland

⁷ School of Mechanical and Electrical Engineering, University of Electronic Science and Technology of China, Chengdu 611731, China

α_T	Coefficient of the total strain energy versus life curve
ε	Strain
κ_p	Exponent of the plastic strain energy versus life curve
κ_T	Exponent of the total strain energy versus life curve

1 Introduction

Advanced high-strength steels with multiphase microstructures have received significant attention in the recent decades due to their excellent combination of strength, ductility, toughness, and wear resistance [1]. These steels, which are formed by the combination of at least two different phases involving ferrite, austenite, martensite or bainite, can be designed to maximise the benefits of each phase and reduce, or even eliminate, the shortcomings of a particular phase, through the presence of the other phases [2]. However, alloy design for these materials is complex and involves not only optimising the elemental composition [3] but also defining a specific heat treatment plan [4] to achieve the desired mechanical properties.

Over the years, substantial progress has been made in enhancing the mechanical properties of advanced high-strength steels through heat treatment processes. Among these new approaches, an example includes the quenching and partitioning (Q–P) process introduced by Speer et al. [2], which creates martensite and carbon-enriched austenite for improved ductility and toughness. Gao et al. [5] found an optimum combination of strength, ductility, and toughness in a medium-carbon Mn–Si–Cr alloyed steel via a bainite-based Q–P process. Zhang et al. [6] proposed a pre-quenching prior to Q–P, in a low-carbon Nb-microalloyed Si–Mn steel, which resulted in higher true stresses when compared to the conventional Q–P process. Gao et al. [7] and Wang et al. [8] proposed a quenching-partitioning-tempering (Q–P–T) process to dig out the effect of precipitation strengthening which led to improved mechanical properties.

Zhao et al. [9] also presented new approach for multiphase low-carbon steels, which involves austempering below the martensite start (M_s) temperature, leading to improved toughness and tensile properties when compared to the classical process based on above- M_s austempering.

In fact, the austempering temperature plays a key role on the desired mechanical properties of advanced high-strength steels. Recent studies [10] have shown that an austempering process performed at a temperature below the martensite start temperature results in better tensile properties than a conventional austempering process performed at a temperature above the martensite start temperature, as it produces low-temperature bainite and

reduces both the size and the volume fraction of the martensite/austenite phases, leading to increased strength. Silva et al. [11] studied the phase transformations during the decomposition of austenite below M_s in a low-carbon steel and explained the kinetics of isothermal bainite formation through a nucleation-based transformation model. Samanta et al. [12] proposed model based on the formation of bainite by displacive mechanism to explain the kinetics of isothermal transformation below M_s .

Although the effect of this new approach to austempering on monotonic tensile properties is well documented, its effect on cyclic deformation has rarely been studied in the open literature. Zhao et al. [13] studied the cyclic deformation behaviour of high-carbon nanobainitic steel elaborated at different tempering temperatures above and below the M_s temperature. These authors found that steel tempered below M_s showed higher volume fraction of retained austenite, resulting in better strain hardening ability than steel tempered above M_s . Yang et al. [14] also examined the effect of tempering temperature on low-cycle fatigue regime in a low-carbon martensitic steel. Although it is not specified if the tempering was done above or below the M_s temperature, the selected tempering temperature greatly impacted the cyclic deformation behaviour. Kumar et al. [15] also reported a significant effect of austempering on nanostructured bainitic steels undergoing fatigue loading.

The limited information mentioned above highlights the need for further research to gain a deeper understanding of the impact of the austempering temperature on the cyclic response of advanced high-strength steels, particularly when it is carried out at temperatures below the martensite start temperature. This is a crucial issue because this class of steel is frequently used in critical engineering components which are subjected to dynamic loading scenarios, namely in critical components of rail and automotive industries, making them vulnerable to fatigue failure [16]. Thus, an effective design against fatigue requires not only a precise description of the cyclic deformation behaviour [17] but also information about the optimum M_s -below tempering temperature [13].

Since this optimum temperature under cyclic loading is not known for multiphase low-carbon steel, the present research aims at studying the influence of M_s -below austempering temperature on cyclic deformation of multiphase low-carbon steel. Another important challenge is the definition of the optimum austempering temperature from a fatigue performance perspective. In order to meet these goals, four different austempering temperatures (190 °C, 230 °C, 275 °C, and 315 °C) below M_s were considered to better understand the dialectical relationship between austempering and fatigue behaviour. Tests were conducted at room temperature under fully reversed strain-controlled conditions with strain amplitudes ranging from 0.5 to 1.0%.

After the tests, fracture surfaces were examined by scanning electron microscopy to characterise fractographic features associated with the different austempering temperatures and strain amplitudes. Microstructural details were analysed by transmission electron microscopy and X-ray diffraction.

2 Materials and methods

2.1 Materials

The material utilised in this study was a three-phase low-carbon steel, whose chemical composition, in weight percentage, is presented in Table 1. The measured martensitic start (M_s) temperature of the tested steel, which represents the highest temperature at which austenite transforms into martensite, was determined to be 353 °C using a Gleeble-3500 thermomechanical simulator [18]. The martensite finish temperature was equal to 178 °C. In order to study the effect of isothermal temperature on cyclic deformation response, four different austempering heat treatments were considered. The steel was austenitised at 930 °C (heated at 10 °C/s) for 45 min and rapidly cooled to different austempering temperatures (190 °C, 230 °C, 275 °C, and 315 °C) at 30 °C/s and isothermally held at each temperature for 2 h. Finally, the steel was quenched to room temperature in air. The interval of austempering temperature was defined

based on a previous study focused on the microstructure and monotonic tensile properties of the tested alloy [19].

2.2 Low-cycle fatigue tests

The low-cycle fatigue tests were performed according to the ASTM E606 standard [20] with cylindrical solid specimens under uniaxial strain-control at strain amplitudes of 0.5%, 0.65%, 0.8% and 1.0%. The maximum and minimum values of strain amplitude were defined in order to ensure (1) fatigue lives higher than 10^3 cycles and (2) the existence of cyclic plastic strain, respectively. It was used a strain ratio (R_ϵ) equal to -1 , a strain rate ($d\epsilon/dt$) equal to $6 \times 10^{-3} \text{ s}^{-1}$, and sinusoidal waves. The specimens were polished to a scratch-free condition with grit sandpaper and 6- μm diamond paste. The gauge section had a diameter of 5 mm and a length of 19 mm. The stress-strain response was recorded with a rate of 200 data points per cycle using a 12.5-mm-long mechanical extensometer connected directly to the gauge section. The tests began in compression and ended at total failure or when the peak stress decreased by 25% relative the maximum stress. A summary of the main stress, strain and energy quantities measured at the half-life cycles as well as the number of reversals to failure is provided in Table 2.

Table 1 Chemical composition of the tested multiphase low-carbon steel (wt%)

C	Mn	Si	Cr	Ni	Mo	Fe
0.18	2.9	1.7	0.8	0.59	0.26	Balance

Table 2 Summary of the low-cycle fatigue tests

Austempering temperature	ϵ_a (%)	$\epsilon_{a,p}$ (%)	σ_a (MPa)	σ_{\max} (MPa)	ΔW_P (MJ/m ³)	ΔW_T (MJ/m ³)	$2N_f$ (reversals)
190 °C	0.5	0.018	961.1	943.7	0.67	2.90	26,344
	0.65	0.101	1094.6	1082.0	2.94	5.97	6812
	0.8	0.197	1198.7	1179.47	6.84	10.43	2976
	1	0.362	1268.0	1229.6	13.47	17.50	1256
230 °C	0.5	0.037	924.8	887.9	0.84	2.87	37,812
	0.65	0.104	1088.9	1040.1	3.69	6.40	7020
	0.8	0.219	1164.2	1126.0	8.14	11.21	3432
	1	0.392	1207.4	1171.8	13.75	17.44	1474
275 °C	0.5	0.039	919.8	854.3	1.29	3.10	24,166
	0.65	0.131	1033.0	993.6	4.13	6.60	6588
	0.8	0.257	1083.5	1049.3	7.49	10.41	3190
	1	0.413	1179.7	1145.1	13.82	17.36	1360
315 °C	0.5	0.025	946.5	883.6	1.25	3.13	18,522
	0.65	0.120	1055.4	1025.2	3.90	6.54	4904
	0.8	0.229	1133.1	1114.9	7.81	11.01	1850
	1	0.407	1178.1	1157.6	13.97	17.60	1176

2.3 Examination of microstructure and fracture surfaces

The microstructure of the tested steels was examined through X-ray diffraction (XRD) and transmission electron microscopy (TEM). X-ray diffraction (XRD) was performed using a Rigaku SmartLab 9 kW XRD system with unfiltered Co-K α radiation (40 kV/135 mA) at a frequency of 3 °/min. TEM analysis was done on specimens thinned by twin-jet electropolishing using a Talos F200S field emission microscope. The fracture surfaces were examined with a Hitachi SU-5000 field emission scanning electron microscope (SEM) in the crack propagation region near the crack initiation sites. Specimens were cut perpendicular to the main axis of the specimen and cleaned in trichloroethylene ultrasonic bath for 10 min.

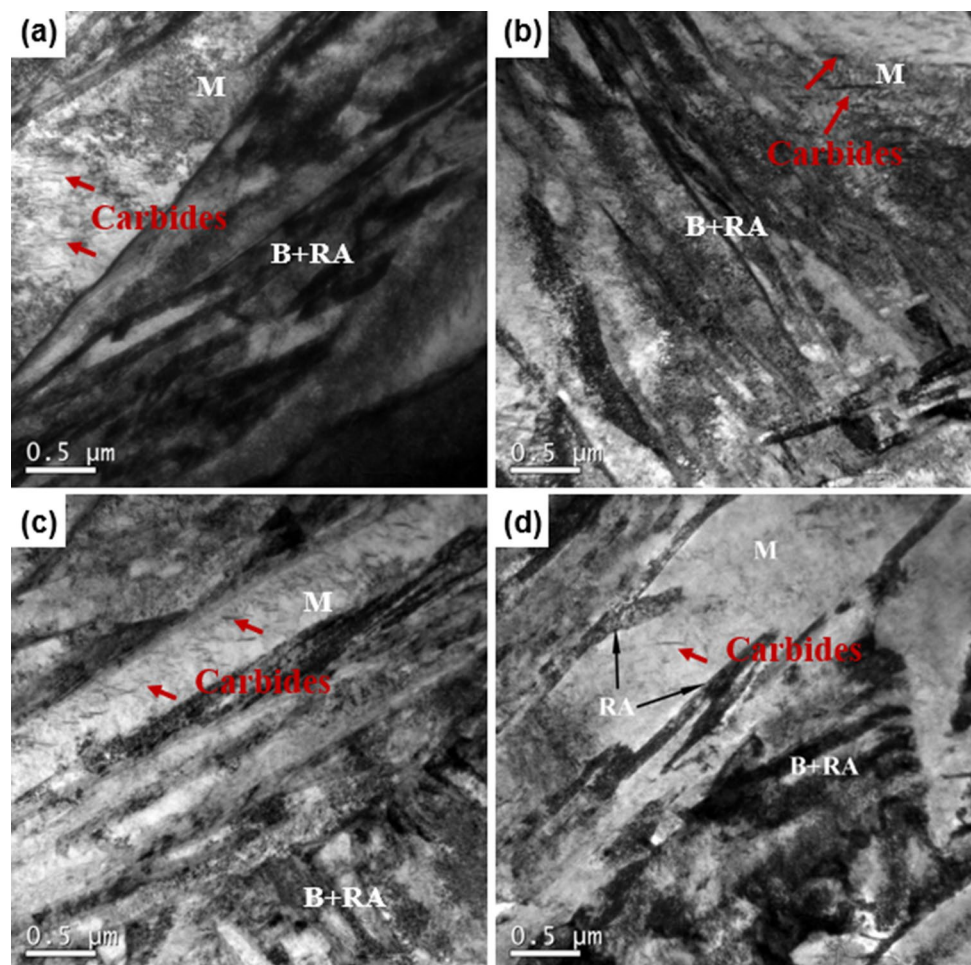
3 Results and discussion

This section is organised into six sub-sections. The first sub-section focuses on microstructural details. The second sub-section examines the cyclic deformation response. The third sub-section tackles the addresses the stress–strain response, while the fourth sub-section explores the fatigue life relations expressed in terms of stress-based, strain-based, and energy-based approaches. The fifth sub-section determines the optimum austempering temperature to achieve improved fatigue performance. Finally, the fracture surfaces are analysed using SEM to identify the main failure mechanisms.

3.1 Microstructure characterisation

The microstructure examined by TEM for the tested multiphase low-carbon steel austempered at different temperatures (190 °C, 230 °C, 275 °C, and 315 °C) below the M_s temperature is shown in Fig. 1a–d, respectively. Overall, this steel exhibits a dominant multiphase bainite/martensite microstructure, mainly composed by bainite, lath martensite,

Fig. 1 TEM micrographs of the three-phase low-carbon steel for different austempering temperatures: **a** 190 °C, **b** 230 °C, **c** 275 °C, and **d** 315 °C (*M* martensite, *RA* retained austenite, *B + RA* bainite and retained austenite)



and retained austenite between the lath martensite [18]. Martensite is formed firstly, showing coarseness in the TEM microstructure. At the same time, during the subsequent phase transformation, martensite will undergo self-tempering and carbides are often distributed on it. This microstructure results in both improved strength and toughness [21]. The highest bainite content was found for the highest austempering temperature (315 °C), where the largest blocky retained austenite was also observed. By contrast, a decrease in austempering temperature led to an increase in martensite content and a reduction in the size of the blocky retained austenite, which became progressively finer [18].

The volume fraction of martensite (V_M) was estimated using the Koistinen–Marburger equation [18]:

$$V_M = 1 - \exp[-0.011 \times (M_s - T)] \quad (1)$$

where M_s is the martensite start temperature, and T is the heat treatment temperature. The volume fraction of bainite (V_B) was calculated as follows:

$$V_B = 1 - V_M - V_{RA} \quad (2)$$

where V_M is volume fraction of martensite and V_{RA} is the volume fraction of retained austenite obtained by X-ray diffraction. The results of these calculations after the different austempering treatments are summarised in Table 3. As shown, the highest bainite content was found at the austempering temperature of 315 °C, decreasing as the austempering temperature decreased. Regarding the volume fraction of martensite, an opposite behaviour was observed, i.e. higher austempering temperatures led to lower values. Xia et al. [18] found a similar relationship between austempering temperature and the volume fractions of bainite and martensite for this alloy steel.

The X-ray diffraction spectrum of the multiphase low-carbon steel austempered at different temperatures below the M_s is exhibited in Fig. 2. As can be seen in the figure, the XRD patterns show two types of peaks, i.e. face-centred cubic (FCC) retained austenite peaks (γ) and body-centred cubic (BCC) martensite/bainite peaks (α). On the other hand, it is evident that the XRD patterns are affected by the austempering temperature, with the retained austenite peaks

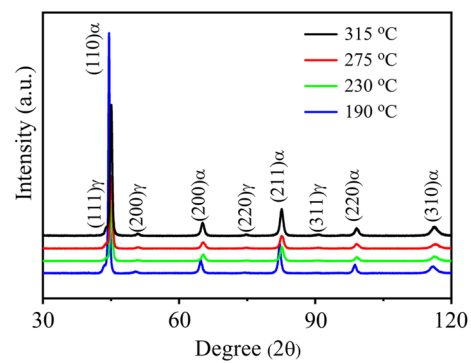


Fig. 2 X-ray diffraction patterns of the three-phase low-carbon steel obtained at different austempering temperatures

becoming more pronounced with increasing austempering temperature, indicating an increase in the retained austenite content [21].

3.2 Cyclic deformation behaviour

The effect of austempering temperature on the cyclic deformation response of the tested steel is shown in Fig. 3. The tests were conducted for the same strain amplitude ($\epsilon_a = 1.0\%$) considering four austempering temperatures. Figure 3a–d shows the stress–strain behaviour collected in the experiments for austempering temperatures of 190 °C, 230 °C, 275 °C, and 315 °C, respectively. For the sake of clarity, the first two cycles and the half-life cycle are highlighted, while the full test is plotted in grey. As shown in the figure, the steel exhibits initial cyclic hardening behaviour in the first cycles, followed by gradual cyclic softening behaviour until total failure, regardless of the austempering temperature. The same trends were found for the other strain amplitudes.

The cyclic response was affected by both the austempering temperature and the strain amplitude. This can be explained by the stability of the retained austenite as well as dislocation state and the microstructural evolution during the cyclic deformation process. In general, cyclic hardening of steels with lower dislocation densities at the initial stage are associated with interaction between the dislocation proliferation and dislocation [18, 22]. On the contrary, for steels with higher dislocation densities, such a behaviour is closely related to the interaction between dislocation during cyclic deformation, leading to the formation of a large number of dislocation tangles and immobile dislocations.

In this steel, the dislocation densities are higher than 10^{15} m^{-2} [18]. Thus, the initial cyclic hardening behaviour is explained by the decrease in the mobile dislocation density. As the cyclic deformation process is ongoing, the accumulated plastic strain induces multi-slip and cross-slip dislocations resulting in a decrease in dislocation density.

Table 3 Volume fractions of martensite, bainite and retained austenite after austempering

Austempering temperature	Volume fraction of martensite, V_M (%)	Volume fraction of bainite, V_B (%)	Volume of retained austenite, V_{RA} (%)
190 °C	80.4	15.3	4.3
230 °C	69.5	23.8	6.7
275 °C	49.6	40.3	10.1
315 °C	22.4	64.3	13.3

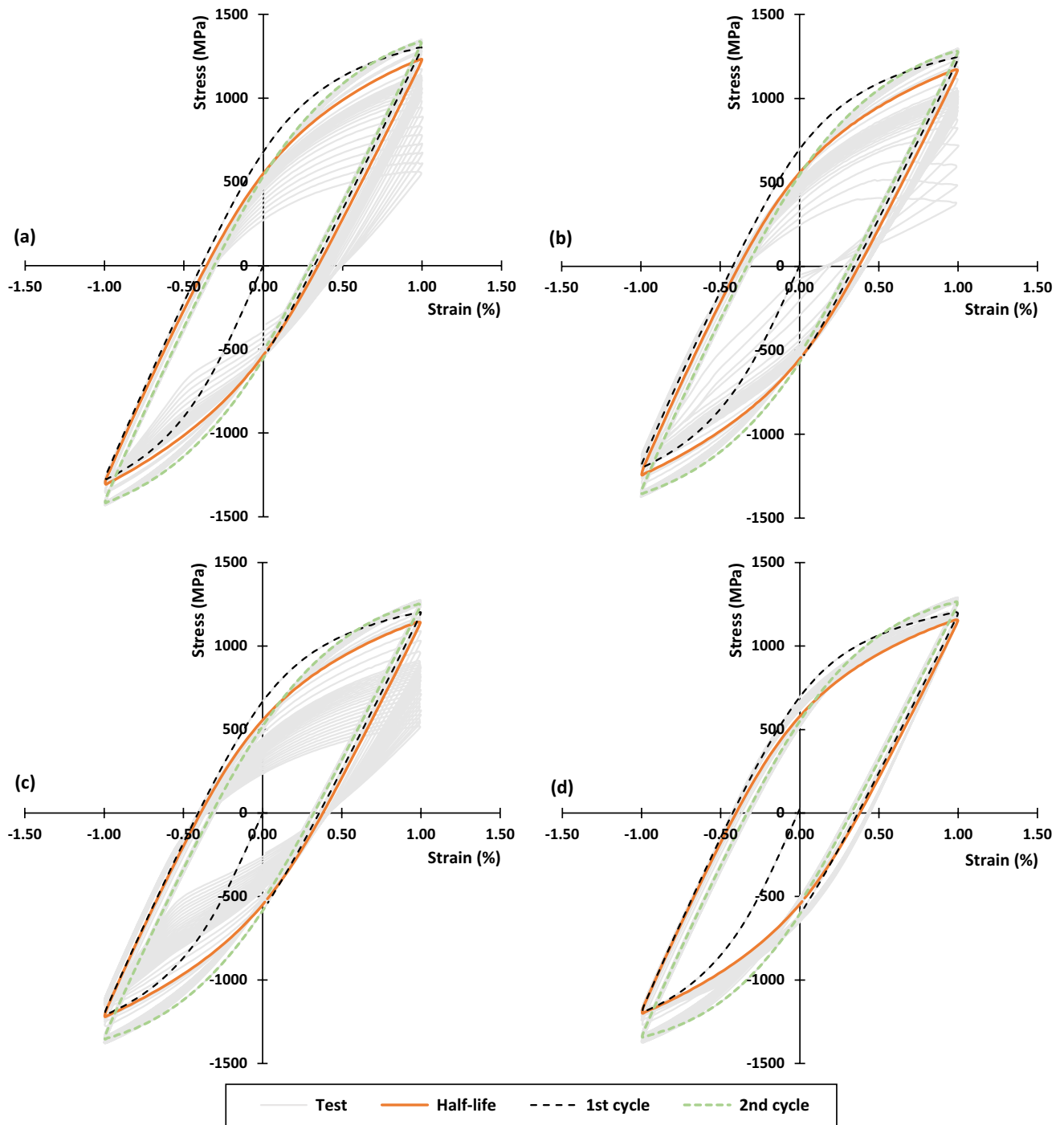


Fig. 3 Cyclic stress–strain response of the tested steel at $\epsilon_a = 1.0\%$ for an austempering temperature of: **a** 190 °C, **b** 230 °C, **c** 275 °C, and **d** 315 °C (*Test* refers to all loops; *Half-life* refers to the loop of the half-

life cycle; *first cycle* refers to the loop of the first cycle; and *second cycle* refers to the loop of the second cycle)

The cyclic softening takes place when the reduction in stress amplitude caused by dislocation annihilation and the formation of low-energy dislocation substructures is higher than the increase in stress amplitude caused by the dislocation tangles and a decrease in mobile dislocation density [18].

The strain amplitude is another parameter that influences the cyclic deformation response of the tested alloy. Figure 4a–d shows, as an example, the stress–strain response at a constant austempering temperature (190 °C) for four strain amplitudes (0.5%, 0.65%, 0.8%, and 1.0%, respectively). To

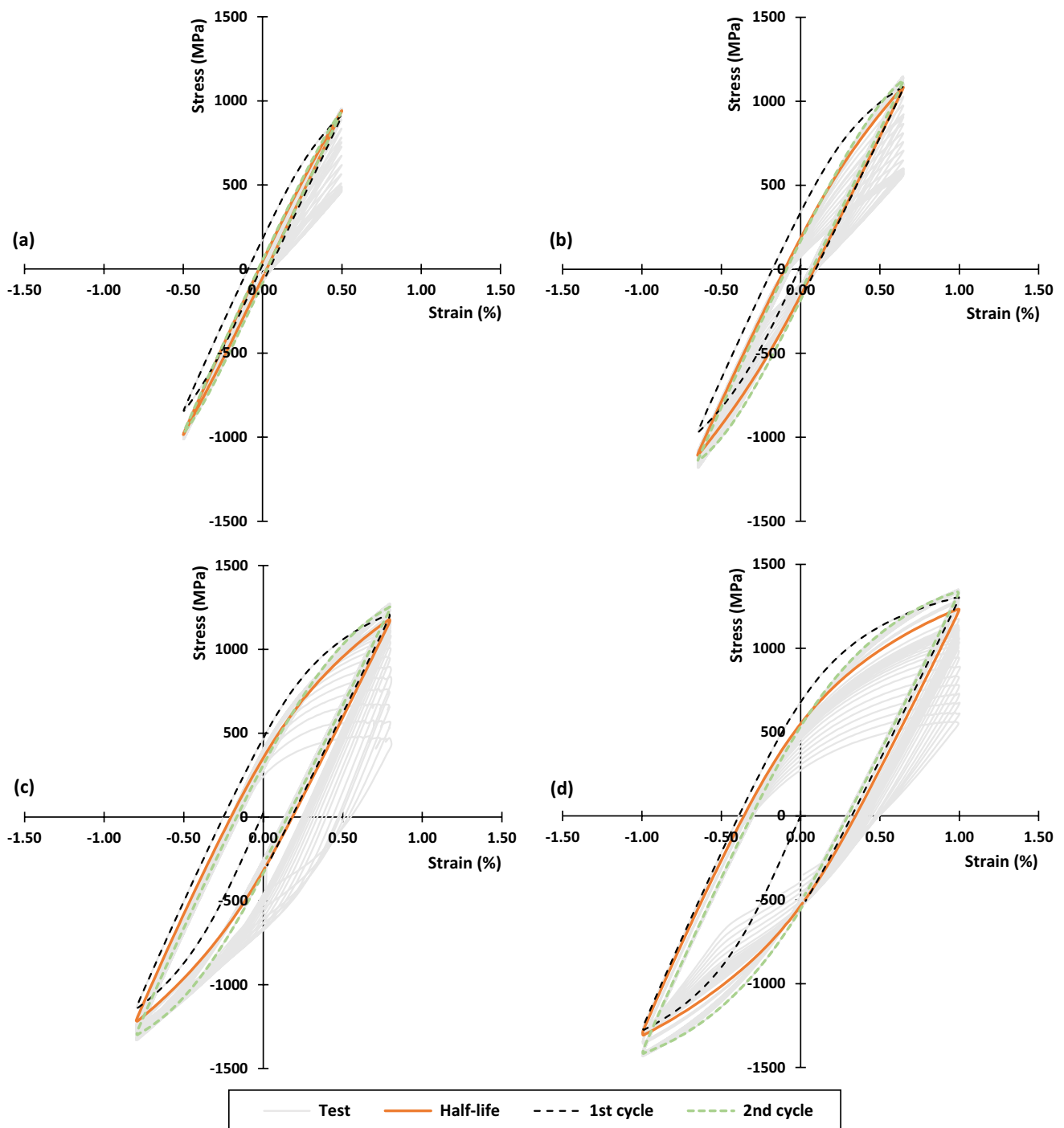


Fig. 4 Cyclic stress–strain response of the tested steel austempered at 190 °C for a strain amplitude (ϵ_a) of: **a** 0.5%, **b** 0.65%, **c** 0.8%, and **d** 1.0% (*Test* refers to all loops; *Half-life* refers to the loop of the half-

life cycle; *first cycle* refers to the loop of the first cycle; and *second cycle* refers to the loop of the second cycle)

make the results clear, the first two cycles and the half-life cycle are highlighted, while the full test is plotted in grey. During the first two cycles, a cyclic hardening behaviour is observed as the maximum tensile stress increases. After the second cycle, the material undergoes gradual cyclic softens

until total failure, leading to a progressive change in the shapes of the hysteresis. These changes are characterised by a reduction in the linear part of both the compressive and the tensile branches. This outcome was consistent across all the austempering temperatures.

The cyclic stress–strain response is generally analysed using dependent parameters, such as the strain amplitude. Figure 5 plots the stress amplitude against the number of cycles for different austempering temperatures and strain amplitudes. Figure 5a compares four strain amplitudes (0.5%, 0.65%, 0.8%, and 1.0%) at two austempering temperatures (190 °C, and 315 °C), while Fig. 5b compares four austempering temperatures (190 °C, 230 °C, 275 °C, and 315 °C) at two strain amplitudes ($\varepsilon_a=0.65\%$, and $\varepsilon_a=1.0\%$). In general, it is clear that this steel cyclically hardens in the first two cycles and then, gradually cyclically softens until total failure, irrespective of the austempering temperature and the strain amplitude.

The cyclic stress–strain response of engineering materials provides valuable insights into their behaviour at varying strain levels. This response is usually characterised through the half-life cycles, which are assumed to represent the stable behaviour [23]. Figure 6 shows the half-life cycles obtained for different austempering temperatures and strain amplitudes. As expected, the shapes of the stress–strain hysteresis loops were influenced by the austempering temperature, which is justified by the microstructural modifications induced by each heat treatment. A graphical comparison of the shapes of the loops for $\varepsilon_a=0.8\%$ is displayed in the figure, see dashed lines. The maximum differences in the areas delimited by the loops relative to the cases austempered at 190 °C were found to be about 9%.

The cyclic stress–strain curve is a vital tool for linking the applied strain with the resulting stress level which is critical for fatigue design purposes [23]. This curve can be expressed as follows [24]:

$$\varepsilon_a = \frac{\sigma_a}{E} + \left(\frac{\sigma_a}{K'} \right)^{\frac{1}{n'}} \quad (3)$$

where K' is the cyclic strain-hardening coefficient, and n' is the cyclic strain-hardening exponent. This curve is generally created by connecting the peak tensile and compressive points of stable stress–strain loops collected at varying strain amplitudes. Table 4 provides the unknowns of Eq. (3) for the four austempering temperatures.

Figure 6a–d exhibits the cyclic stress–strain curves calculated for the advanced high-strength steel austempered at various temperatures (190 °C, 230 °C, 275 °C, and 315 °C, respectively). The results show that the proposed functions accurately reflect the cyclic elastic–plastic behaviour of the tested steel, either for the tensile or the compressive branches. The maximum discrepancies between the peak tensile and compressive points of the hysteresis loops and the corresponding stresses obtained using the cyclic curve were 2.5%, 4.7%, 6.8% and 6.3%, respectively, for austempering temperatures of 190 °C, 230 °C, 275 °C, and 315 °C.

The shape of the hysteresis loops is a crucial aspect from the perspective of fatigue design of engineering materials. Although the cyclic stress–strain curve can correlate both the applied stress and the corresponding strain level, it fails to depict the shape of the hysteresis loop. Based on the shape of the hysteresis loops, metallic materials are generally classified into Masing and non-Masing [25]. Masing materials are those whose hysteresis loop branches can be derived from the cyclic stress–strain curve multiplied by a factor of two, while non-Masing materials are those that do not follow this criterion [23].

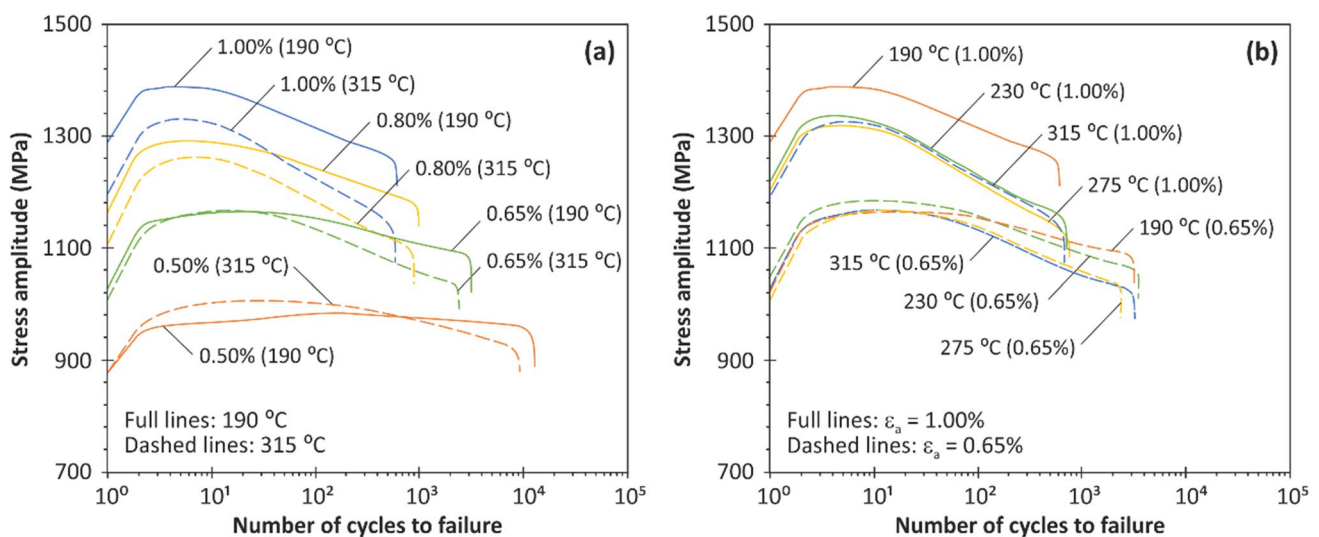


Fig. 5 Stress amplitude versus number of cycles to failure: **a** four strain amplitudes (1.0% and 0.65%) at two austempering temperatures (190 °C, and 315 °C); **b** four austempering temperatures (190 °C, 230 °C, 275 °C, and 315 °C) at two strain amplitudes (1.0%, and 0.65%); and (b)

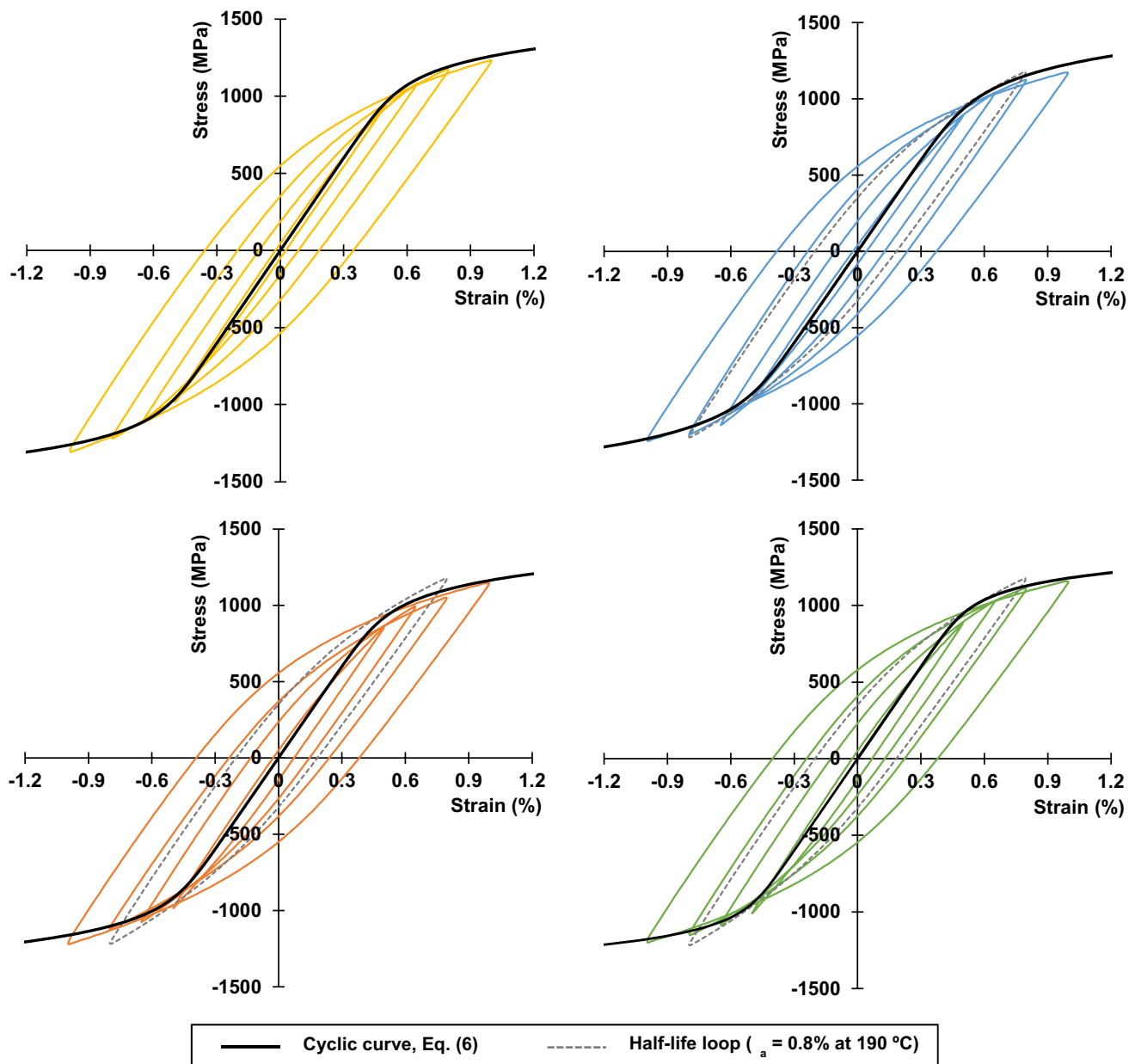


Fig. 6 Cyclic stress–strain curves of the tested steel for different austempering temperatures: **a** 190 °C; **b** 230 °C; **c** 275 °C; and **d** 315 °C

Table 4 Constants of the cyclic stress–strain curves

Austempering temperature	K' (MPa)	n'	R^2
190°C	2108.1	0.0918	0.984
230°C	2300.1	0.1129	0.964
275°C	2020.2	0.1008	0.974
315°C	1826.7	0.0798	0.992

Figure 7a–d displays the Masing-type curves (represented by the solid lines) for various austempering temperatures (190 °C, 230 °C, 275 °C, and 315 °C, respectively) as well as the corresponding stable hysteresis loops in relative coordinates (i.e. with the compressive tips moved to the origin of the referential system). As seen, the upper branches of the curves do not overlap perfectly, indicating that these materials are non-Masing. However, the deviation is not significant, and a Masing-type approach can reasonably describe the hysteresis loop shapes for the strain amplitudes and austempering temperatures studied in this research.

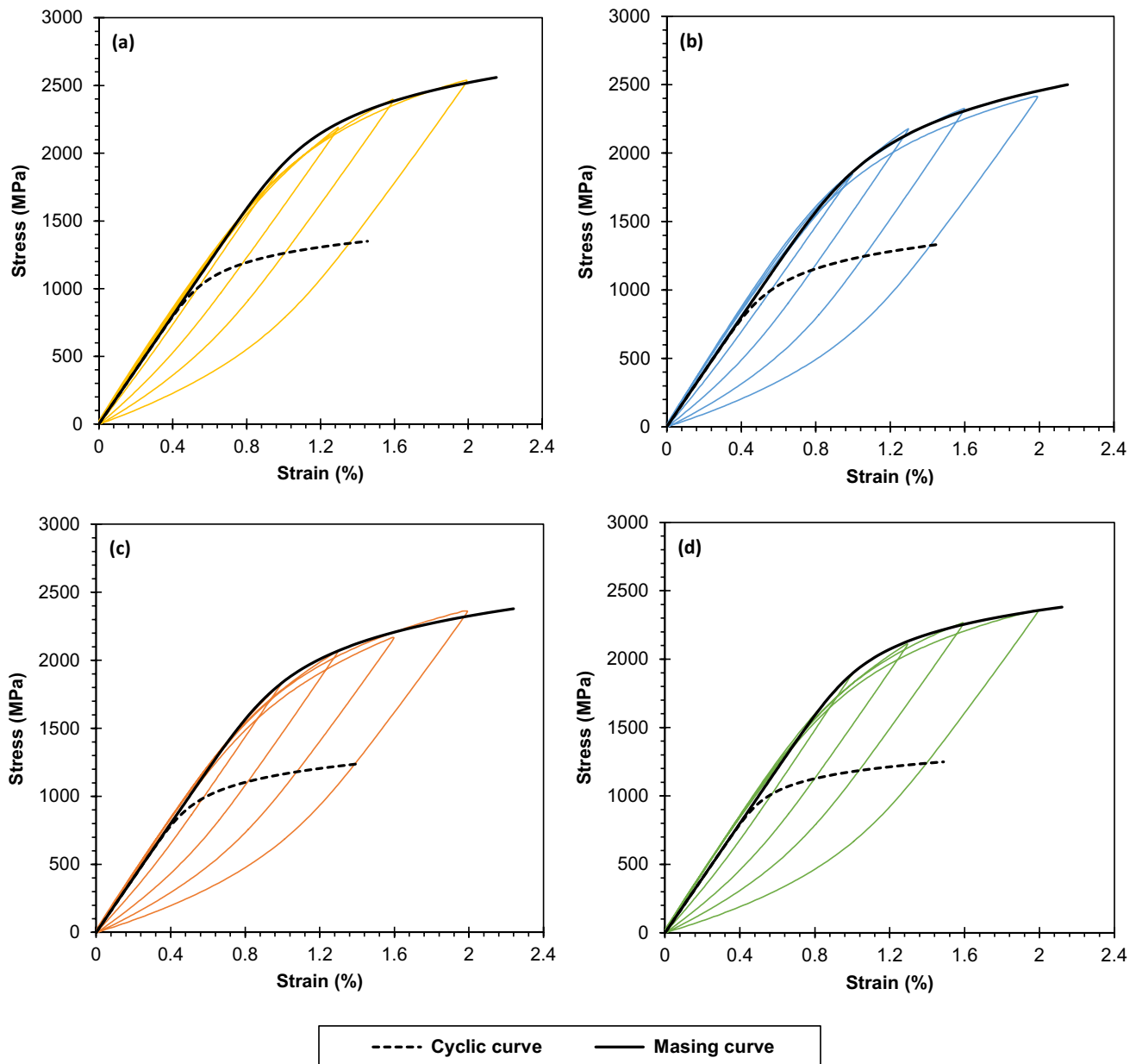


Fig. 7 Stable stress–strain loops and Masing-type curves of the tested steel at different austempering temperatures: **a** 190 °C; **b** 230 °C; **c** 275 °C; and **d** 315 °C

A careful examination of Fig. 7 reveals that the linear portion of the hysteresis loops is not constant, supporting the behaviour described above. The variation in the linear portion of the hysteresis loops is associated with the dislocation density and cell size [19]. In a perfect Masing-type material, the deformation structure is unaffected by strain amplitude or dislocation motion, remaining stable under fatigue loading. By contrast, the non-Masing behaviour arises from changes in microstructure, due to applied strain amplitude and heat treatment, which interferes with the cell structure and eases the motion of dislocations [26]. The dislocation

density of the steel under study increased with increasing strain amplitudes, regardless of the austempering temperature, which is consistent with the reported results [27].

3.3 Fatigue life

Fatigue design approaches are generally formalised using stress-based, strain-based, or energy-based relationships [23]. Stress-based approaches are ideal for the high-cycle fatigue, where cyclic plasticity occurs in localised regions. Strain-based approaches are better for the low-cycle

fatigue, where significant plastic deformation exists. Energy-based approaches, which combine both stress and strain components, are often used in both regimes due to their unifying character.

The fatigue life relationships for the tested cases expressed through stress-based, strain-based, and energy-based approaches are plotted in Fig. 8. Regarding the stress-life relationships, the Basquin equation, which relates the stress amplitude (σ_a) against the number of reversals to failure ($2N_f$), is widely used in fatigue design [28]:

$$\sigma_a = \sigma'_f (2N_f)^b \quad (4)$$

where σ_a is the stress amplitude, $2N_f$ is the number of reversals to failure, σ'_f is the fatigue strength coefficient, and b is the fatigue strength exponent. The two constants for the various austempering temperatures are listed in Table 5.

Figure 8a plots the stress-life relationships for the tested steel at different austempering temperatures. As shown, these relationships were affected by the austempering temperature. The curves for higher temperatures (275 °C and 315 °C) were similar for the entire range, while the curves for lower temperatures (190 °C and 230 °C) were close for longer lives but diverged slightly as the lifetime decreased.

Concerning the strain-life relationships, the Manson–Coffin–Basquin equation is often used. This equation is defined as follows [28–30]:

$$\varepsilon_a = \frac{\sigma'_f}{E} (2N_f)^b + \varepsilon'_f (2N_f)^c \quad (5)$$

where ε_a is the strain amplitude, σ'_f is the fatigue strength coefficient, E is the Young's modulus, $2N_f$ is the number of reversals to failure, b is the fatigue strength exponent, ε'_f is the fatigue ductility coefficient, and c is the fatigue ductility exponent. The constants for the tested cases are summarised in Table 5.

Figure 8b displays the strain-life relationships for the steels under study at different austempering temperatures. At the highest austempering temperature, i.e. 315 °C, the fatigue life for a given strain amplitude was lower than the other cases. The best fatigue performance was achieved at an austempering temperature of 230 °C. In the remaining two cases, i.e. 190 °C and 275 °C, the strain-life curves were comparable, resulting in intermediate fatigue performance.

Energy-life relationships are often used in fatigue design problems involving high-strength steels, either under uniaxial [31] or multiaxial loading [32]. One of the most widely used models for this purpose is the Smith–Watson–Topper (SWT) model [33]:

$$\sigma_{\max} \varepsilon_a = \frac{\sigma_f'^2}{E} (2N_f)^{2b} + \sigma_f' \varepsilon_f' (2N_f)^{b+c} \quad (6)$$

where σ_{\max} is the maximum tensile stress, and ε_a is the strain amplitude acting on the critical plane, σ_f' is the fatigue strength coefficient, E is the Young's modulus, $2N_f$ is the number of reversals to failure, b is the fatigue strength exponent, ε_f' is the fatigue ductility coefficient, and c is the fatigue ductility exponent. The constants calculated for the steels under study are outlined in Table 5.

Figure 8c exhibits the evolution between the SWT parameter and the number of reversals to failure for the studied cases. The best fatigue performance was found with an austempering temperature of 230 °C, while the lowest fatigue performance was observed at 315 °C. The steel austempered at 190 °C had a fatigue performance close to that of 230 °C, and the steel austempered at 275 °C the fatigue performance had fatigue performance close to that of 315 °C. However, there is some scatter in the SWT-life functions at both low and high fatigue lives, making the effect of the austempering temperature less clear.

Liu's model is another commonly used approach for predicting the fatigue life based on energy concepts. This model is formalised through the virtual strain energy density applied in the component [34]:

$$\Delta W = \Delta \sigma \Delta \varepsilon = \frac{4\sigma_f'^2}{E} (2N_f)^{2b} + 4\sigma_f' \varepsilon_f' (2N_f)^{b+c} \quad (7)$$

where $\Delta \sigma$ is the stress range, and $\Delta \varepsilon$ is the strain range, σ_f' is the fatigue strength coefficient, E is the Young's modulus, $2N_f$ is the number of reversals to failure, b is the fatigue strength exponent, ε_f' is the fatigue ductility coefficient, and c is the fatigue ductility exponent. Table 5 lists the values of the fitted constants for the studied cases.

Figure 8d presents the energy-life functions obtained for different austempering temperatures using the Liu's parameter. In general, the conclusions are very similar to those for the SWT parameter, i.e. steel austempered at 230 °C had the best fatigue performance while the worst was seen at 315 °C. The two remaining temperatures (i.e. 190 °C, and 275 °C) showed intermediate performance with the former slightly better than the latter. In addition, it is also visible some scatter, especially at low and high fatigue lives, making the effect of the austempering temperature not completely perceptible.

Other popular energy-based formulations are built on the concept of strain energy density, such as the plastic strain energy density or the total strain energy density. The plastic strain energy density (ΔW_p), which reflects the area of the hysteresis loop, is effective in addressing low-cycle fatigue problems under fully-reversed or almost fully-reversed conditions. However, its inability to deal with mean stress effects

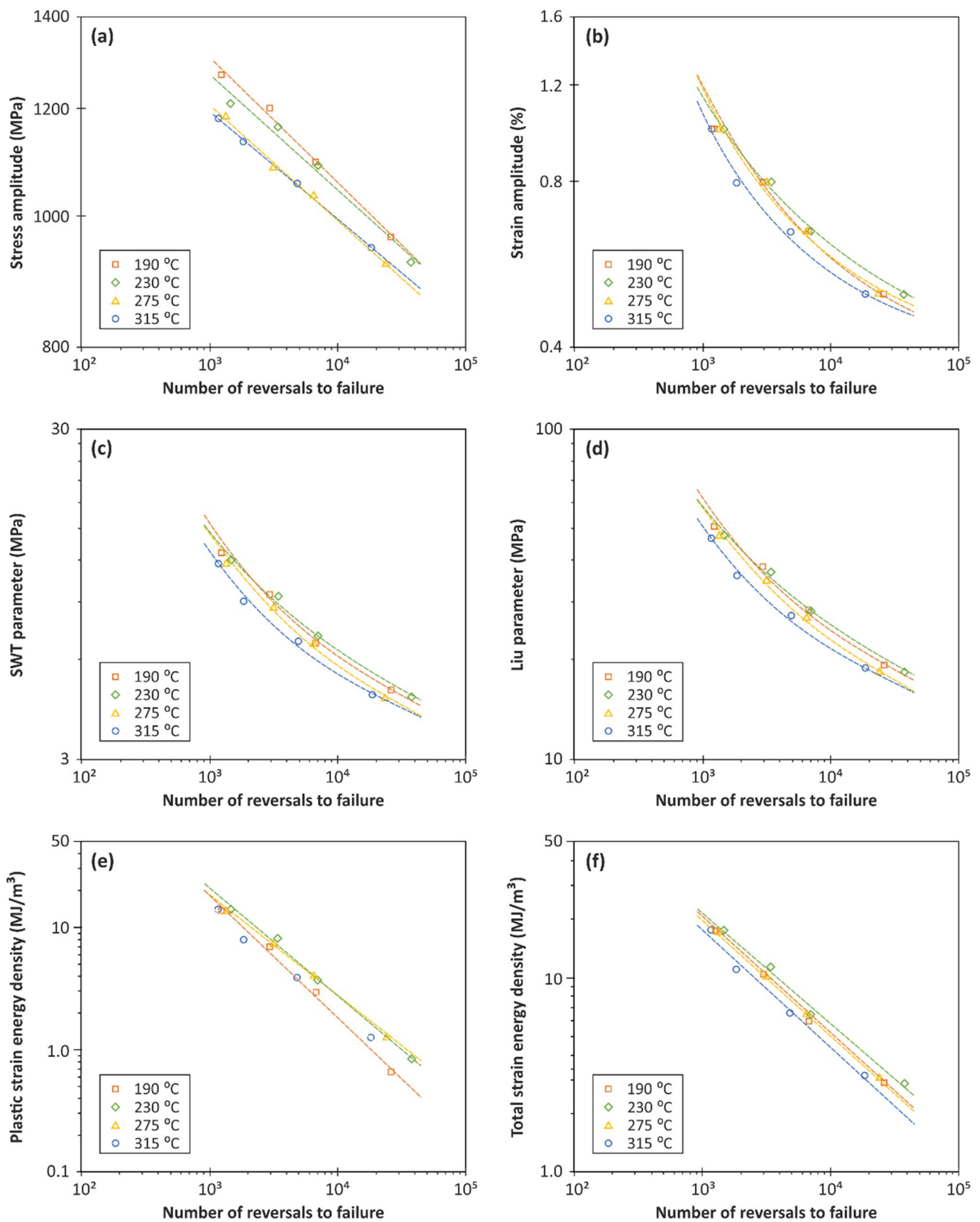


Fig. 8 Fatigue life relationships for the different austempering temperatures defined through: **a** stress amplitude; **b** strain amplitude; **c** SWT parameter; **d** Liu's parameter; **e** plastic strain energy density;

and **f** total strain energy density. Total strain energy density defined by the sum of both the plastic and the positive elastic components

Table 5 Constants of the stress-life relationships

Austempering temperature	σ'_f (MPa)	B	R^2	ϵ'_f	c	R^2
190 °C	2471	-0.0921	0.992	4.948	-0.9891	0.979
230 °C	2278	-0.0846	0.978	0.842	-0.7397	0.995
275 °C	2180	-0.0855	0.996	1.870	-0.8333	0.972
315 °C	2054	-0.0787	0.999	4.009	-0.9765	0.985

Table 6 Constants of the plastic strain energy density versus life relationships

Austempering temperature	α_p (MJ/m ³)	κ_p	R^2
190 °C	1204.9	-0.595	0.999
230 °C	1048.9	-0.564	0.993
275 °C	1299.5	-0.599	0.999
315 °C	1128.2	-0.602	0.971

Table 7 Constants of the total strain energy density versus life relationships

Austempering temperature	α_T (MJ/m ³)	κ_T	ΔW_{0_T} (MJ/m ³)	R^2
190 °C	2144.2	-0.691	0.76	0.997
230 °C	2108.1	-0.670	0.81	0.991
275 °C	2004.2	-0.691	0.76	0.989
315 °C	2106.9	-0.705	0.65	0.991

limits its widespread application. It can be expressed through the following equation [23]:

$$\Delta W_p = \alpha_p (2N_f)^{\kappa_p} \quad (8)$$

where ΔW_p is the plastic strain energy density, α_p and κ_p are material constants, and $2N_f$ is the number of reversals to failure. The values of these two constants for the tested materials are presented in Table 6.

Figure 8e shows the relationship between the plastic strain energy density and the fatigue life for the different austempering temperatures. As depicted, the plastic strain energy density decreased as the fatigue life increased, but there was no clear correlation between the austempering temperature and the values of ΔW_p . The highest fatigue performance was achieved at an austempering temperature of 230 °C. The results at 275 °C were relatively similar. Regarding the two remaining austempering temperatures, i.e. 190 °C and 315 °C, the fatigue lives were lower when compared to the other cases.

Concerning the total strain energy density, it is defined as the sum of both the plastic and the elastic components. This unifying characteristic enables its use under low-cycle and the high-cycle fatigue loading. In particular, the formulation introduced by Ellyn, which takes into account the positive elastic and the plastic strain energy density components, is sensitive to mean stress effects making it advantageous. This formulation can be written as follows [23]:

$$\Delta W_T = \alpha_T (2N_f)^{\kappa_T} + \Delta W_0^+ \quad (9)$$

where ΔW_T is the total strain energy density, α_T and κ_T are material constants, ΔW_0^+ represents the tensile elastic energy at the material fatigue limit, and $2N_f$ is the number of

reversals to failure. The fitted constants for the tested materials are presented in Table 7.

Figure 8f plots the total strain energy density against the number of reversals to failure for the various austempering temperatures. The results suggest that the austempering temperature has little effect on the slope of the curves. However, each curve holds a unique position. This seems to indicate that the total strain energy density is sensitive to the austempering temperature, making this parameter ideal to explore the relationships between fatigue life and austempering temperature for this steel. A careful examination of the figure shows that the best fatigue performance was attained at an austempering temperature of 230 °C, while the weakest performance was observed at an austempering temperature of 315 °C. For the other two temperatures, i.e. 190 °C and 275 °C, the energy-life curves were comparable and provided a moderate fatigue performance.

3.4 Influence of tempering temperature on fatigue life

The influence of austempering temperature on fatigue life in the low-cycle fatigue regime for this steel, as documented in the previous section, is complex. Thus, the development of an austempering temperature-dependent model can help designers to better understand the relationship between durability and austempering temperature. In this study, we used the same approach proposed by Yang et al. [14] for advanced low-carbon steels, but here it is formalised using the total strain energy density (see Eq. 9), instead of using the plastic strain energy density, since the former parameter was sensitive to the austempering temperature (see Eq. 8). Here, the dependency between the material constants and the

austempering temperature was established using third-order polynomial functions:

$$\varphi(T) = c_1 T^3 + c_2 T^2 + c_3 T + c_4 \tag{10}$$

where $\varphi(T)$ represents the material constants associated with the total strain energy density model (i.e. α_T, κ_T , and ΔW_0^+), c_i are fitting constants, and T is the austempering temperature.

Figure 9 displays the correlation between the fatigue life and the austempering temperature for constant values of total strain energy density. For the sake of comparability, the fatigue life (N_f) was divided by the fatigue life at 230 °C (N'_f). As shown, it is evident that the austempering temperature affects fatigue durability. The optimum austempering temperature (i.e. the austempering temperature associated with the maximum fatigue life at a given value of ΔW_T) for the range of total strain energy density under study is relatively consistent and falls between 230 and 244 °C. Any deviation from the optimum austempering temperature, whether an increase or decrease, has a negative impact on fatigue performance and results in a sudden decrease in fatigue life.

The optimum austempering values for the tested steel are represented by the solid black line in Fig. 9. It is clear that when the fatigue life decreases or the total strain energy density increases, the optimum austempering temperature slightly rises. By contrast, when the fatigue life increases or the total strain energy density decreases, the optimum austempering temperature slightly diminishes. The relationship between the total strain energy density (ΔW_T) and the

optimum austempering temperature (T_{opt}) as be expressed as follows:

$$\Delta W_T = a_1 (T_{opt})^3 + a_2 (T_{opt})^2 + a_3 (T_{opt}) + a_4 \tag{11}$$

where ΔW_T is the total strain energy density, a_i are fitting constants, whose values are listed in Table 8, and T_{opt} is the optimum austempering temperature.

At the same value of total strain energy density, defined here as the sum of both the elastic and plastic components, the higher is the yield strength, the higher is the elastic component of the total strain energy density. Since the fatigue life depends on the plastic component, the increase in the yield strength is expected to result in a longer fatigue life. Thus, because the yield strength is higher for lower austempering temperatures, see Table 9, the optimum austempering temperature tends to decrease, as the austempering temperature decreases, see Fig. 9. On the other hand, for a high level of total strain energy density, the ratio of the plastic component to the total strain energy density increases, and a steel with higher ductility generally exhibits a higher life. At higher values of the total strain energy density, as shown in Table 9, the ductility decreases for lower austempering temperatures, which is detrimental for an improved fatigue life. Therefore, in this case, the optimum austempering temperature tends to increase for greater austempering temperatures, see Fig. 9.

3.5 Fractography analysis

The fractographic analysis of the tested steel was performed at both low strain amplitude ($\epsilon_a = 0.5\%$) and high strain amplitude ($\epsilon_a = 1.0\%$) through scanning electron microscopy. Figure 10a–d shows the SEM micrographs at low strain amplitudes for the austempering temperatures of 190 °C, 230 °C, 275 °C, and 315 °C, respectively, while Fig. 11a–d shows the SEM micrographs at high strain amplitudes for the austempering temperatures of 190 °C, 230 °C, 275 °C, and 315 °C, respectively.

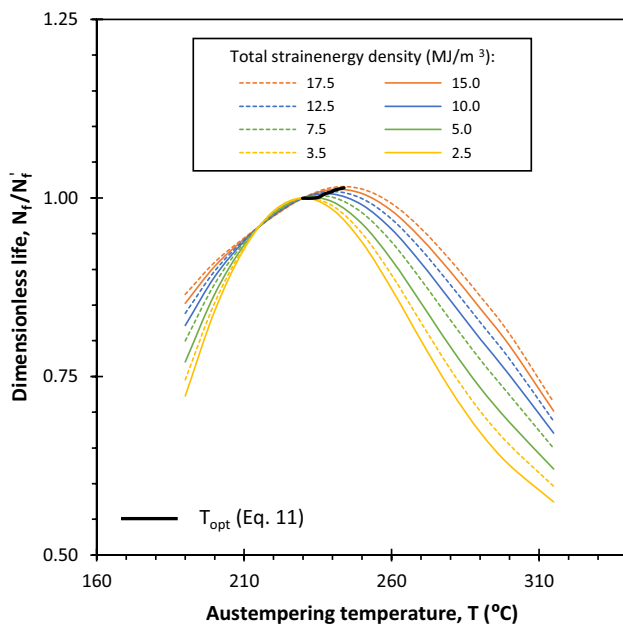


Fig. 9 Relationship between optimum austempering temperature and fatigue life at constant values of total strain energy density

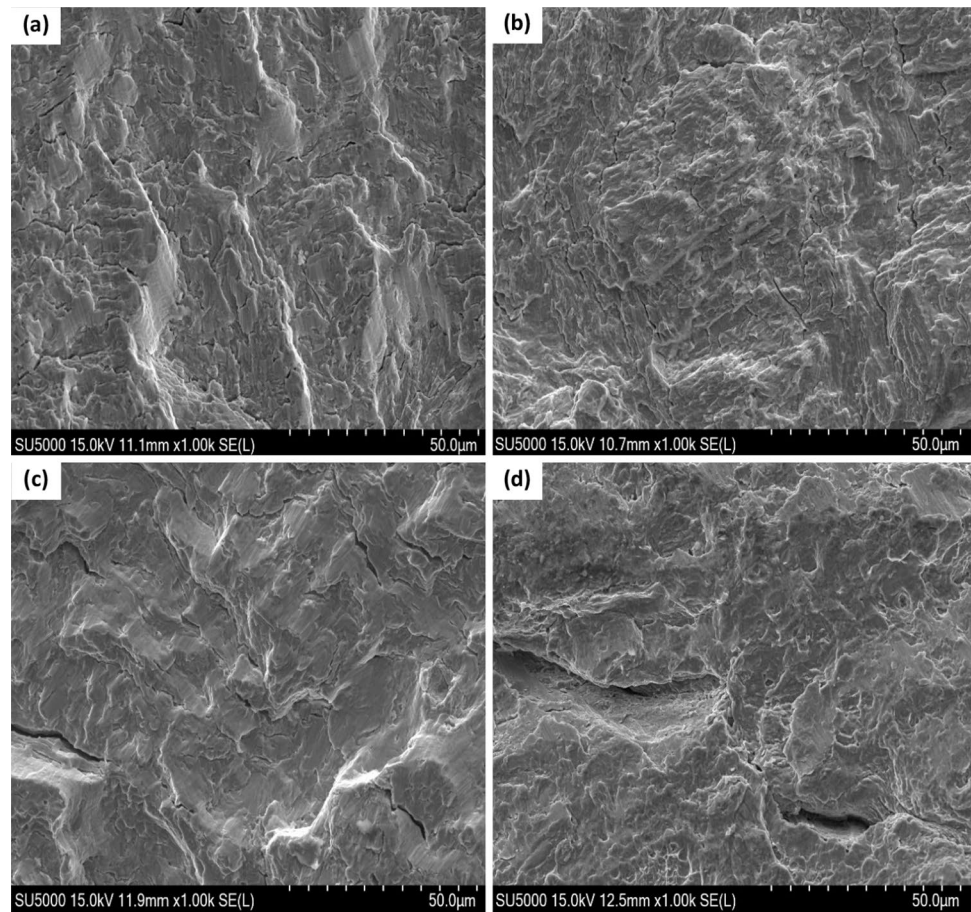
Table 8 Constants of Eq. (11)

a_1 (MJ/m ³)	a_2 (MJ/m ³)	a_3 (MJ/m ³)	a_4 (MJ/m ³)
2.777×10^{-3}	1.985	-4.718×10^2	3.729×10^4

Table 9 Yield strength and elongation for the different austempering temperatures

Mechanical property	190 °C	230 °C	275 °C	315 °C
Yield strength, YS (MPa)	1535	1534	1466	1441
Uniform elongation, δ (%)	7.12	5.57	5.20	4.83

Fig. 10 SEM micrographs at $\epsilon_a=0.5\%$ for the different austempering temperatures of: **a** 190 °C; **b** 230 °C; **c** 275 °C; and **d** 315 °C



At low strain amplitude ($\epsilon_a=0.5\%$), see Fig. 10, the striation area displayed obviously brittle characteristics mainly dominated by cleavage facets (for the lowest austempering temperature) and secondary cracks with some evidence plastic deformation (in the form of micro-dimples). On the contrary, at high strain amplitude ($\epsilon_a=1.0\%$), see Fig. 11, secondary cracks were wider and longer (due to higher tensile stress level) and there were more ductile dimples as well as more evidence of plastic deformation.

The effect of austempering temperature on fracture surfaces was also evident. At the highest austempering temperatures (275 °C, and 315 °C), the surface morphologies are relatively similar and are characterised by more and longer secondary cracks. By contrast, at the lowest austempering temperatures (190 °C, and 230 °C), the two surface morphologies are also consistent and exhibit less and smaller secondary cracks as well as smaller cleavage-like facets. These differences are in line with the fatigue life results and can be attributed to the microstructural changes caused by the austempering temperature.

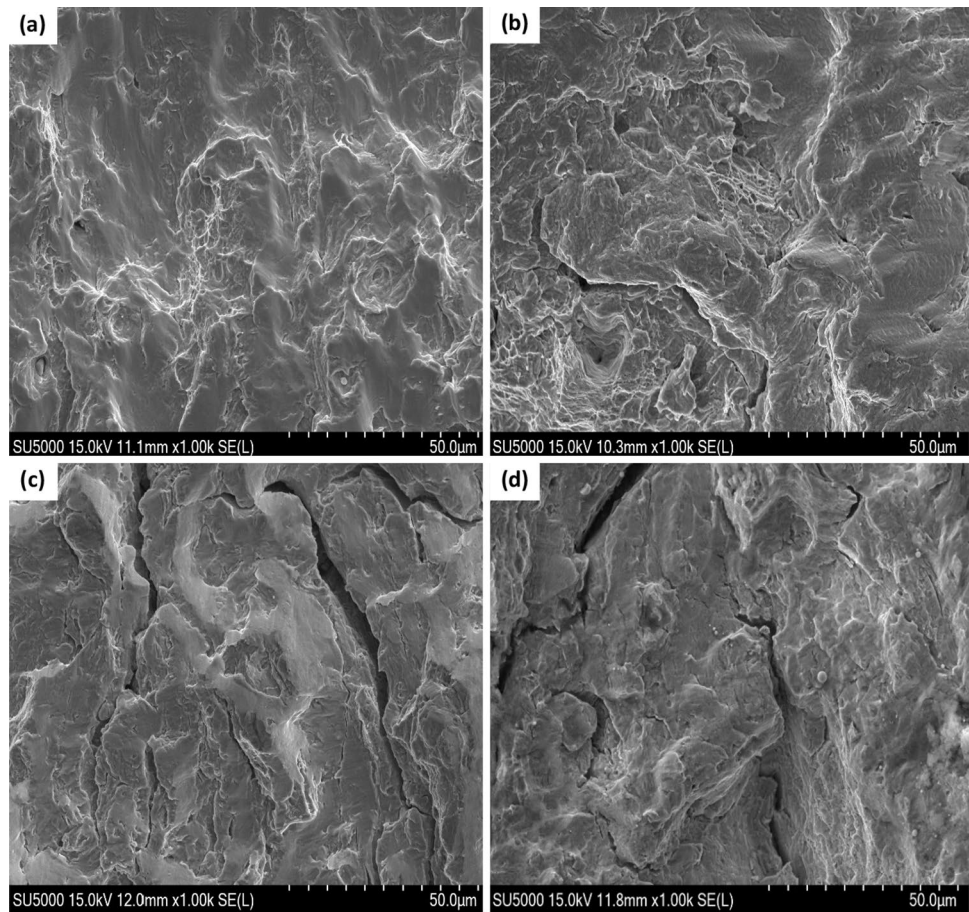
4 Conclusions

This paper investigated the effect of austempering temperature below the martensite start temperature on the cyclic deformation behaviour of multiphase low-carbon steel. The tests were performed at room temperature with strain amplitudes of 0.5–1.0% under fully reversed strain-controlled conditions. Four austempering temperatures were considered:

190 °C, 230 °C, 275 °C, and 315 °C. The study also analysed the microstructure and the failure mechanisms for each austempering temperature. The following conclusions can be drawn:

- The tested multiphase low-carbon steel exhibited a microstructure of bainite/martensite, primarily composed by bainite, lath martensite, and retained austenite. The higher content of bainite was found for the higher austempering temperatures;
- The cyclic deformation response was characterised by a cyclic hardening behaviour during the first two cycles

Fig. 11 SEM micrographs at $\epsilon_a = 1.0\%$ for the different austempering temperatures of: **a** 190 °C; **b** 230 °C; **c** 275 °C; and **d** 315 °C



followed by progressive cyclic softening until failure, regardless of the tested conditions;

- Stress-based, strain-based, and energy-based relations were affected by the austempering temperature. All selected parameters indicated the best fatigue performance at 230 °C and worst fatigue performance at 315 °C;
- The optimum austempering temperature was dependent on the total strain energy density generated during the loading scenario and varied within the range 230–244 °C. It increased for higher energy levels (i.e. lower fatigue lives) and vice-versa.

Acknowledgements This research is sponsored by FEDER funds through the program COMPETE—Programa Operacional Factores de Competitividade—and by national funds through FCT—Fundação para a Ciência e a Tecnologia—under the project UIDB/00285/2020 and LA/P/0112/2020. The authors also would like to thank Carlos Barreira, master's student from the University of Coimbra.

Declarations

Conflict of interest Authors declare that they has no conflict of interest;

Ethical approval This article does not contain any studies with human participants or animals performed by any of the authors.

Open Access This article is licensed under a Creative Commons Attribution 4.0 International License, which permits use, sharing, adaptation, distribution and reproduction in any medium or format, as long as you give appropriate credit to the original author(s) and the source, provide a link to the Creative Commons licence, and indicate if changes were made. The images or other third party material in this article are included in the article's Creative Commons licence, unless indicated otherwise in a credit line to the material. If material is not included in the article's Creative Commons licence and your intended use is not permitted by statutory regulation or exceeds the permitted use, you will need to obtain permission directly from the copyright holder. To view a copy of this licence, visit <http://creativecommons.org/licenses/by/4.0/>.

References

1. Caballero FG, Bhadeshia HKDH. Very strong bainite. *Curr Opin Solid State Mater Sci.* 2004;8:251–7.
2. Speer J, Matlock DK, Cooman BCD, Schroth JG. Carbon partitioning into austenite after martensite transformation. *Acta Mater.* 2003;51:2611–22.

3. Long XY, Zhang FC, Zhang CY. Effect of Mn content on low-cycle fatigue behaviors of low-carbon bainitic steel. *Mater Sci Eng A*. 2017;697:111–8.
4. Wang X, Liu C, Qin Y, Li Y, Yang Z, Long X, Wang M, Zhang FC. Effect of tempering temperature on microstructure and mechanical properties of nanostructured bainitic steel. *Mater Sci Eng A*. 2022;832: 142357.
5. Gao GH, Zhang H, Tan ZL, Liu WB, Bai BZ. A carbide-free bainite/martensite/austenite triplex steel with enhanced mechanical properties treated by a novel quenching-partitioning-tempering process. *Mater Sci Eng A*. 2013;559:165–9.
6. Zhang J, Ding H, Misra RDK, Wang C. Enhanced stability of retained austenite and consequent work hardening rate through pre-quenching prior to quenching and partitioning in a Q-P microalloyed steel. *Mater Sci Eng A*. 2014;611:252–6.
7. Gao GH, Zhang H, Gui XL, Luo P, Tan ZL, Bai BZ. Enhanced ductility and toughness in an ultrahigh-strength Mn-Si-Cr-C steel: the great potential of ultrafine filmy retained austenite. *Acta Mater*. 2014;76:425–33.
8. Wang XD, Zhong N, Rong YH, Hsu TY. Novel ultrahigh-strength nanolath martensitic steel by quenching-partitioning-tempering process. *J Mater Res*. 2009;24:260–7.
9. Zhao LJ, Qian LH, Meng JY, Zhou Q, Zhang FC. Below-Ms austempering to obtain refined bainitic structure and enhanced mechanical properties in low-C high-Si/Al steels. *Scr Mater*. 2016;112:96–100.
10. Yang ZN, Zhang FC, Ji YL, Wang YH, Lv B, Wang ML. Notably improved mechanical properties via introducing a short austempering treatment on lowcarbon martensite steel. *Mater Sci Eng A*. 2016;673:524–9.
11. Silva EPD, Xu W, Föjler C, Houbaert Y, Sietsma J, Petrov RH. Phase transformations during the decomposition of austenite below Ms in a low-carbon steel. *Mater Charact*. 2014;95:85–93.
12. Samanta S, Biswas P, Giri S, Singh SB, Kundu S. Formation of bainite below the Ms temperature: kinetics and crystallography. *Acta Mater*. 2016;105:390–403.
13. Zhao X, Zhang FC, Yang Z, Zhao J. Cyclic deformation behavior and microstructure evolution of high-carbon nano-bainitic steel at different tempering temperatures. *Mater Sci Eng A*. 2019;751:323–31.
14. Yang G, Xia SL, Zhang FC, Branco R, Long XY, Li YG, Li JH. Effect of tempering temperature on monotonic and low-cycle fatigue properties of a new low-carbon martensitic steel. *Mater Sci Eng A*. 2021;826: 141939.
15. Kumar A, Blessto B, Singh A. Effect of austempering temperature on high cycle fatigue behaviour in nanostructured bainitic steels. *Mater Sci Eng A*. 2022;846: 143269.
16. Deng QY, Zhu SP, He JC, Li XK, Carpinteri A. Multiaxial fatigue under variable amplitude loadings: review and solutions. *Int J Struct Integr*. 2022;13:349–93.
17. Lv B, Xia S, Zhang FC, Yang G, Long XL. Comparison of novel low-carbon martensitic steel to maraging steel in low-cycle fatigue behavior. *Coatings*. 2022;12:818.
18. Xia S, Zhang FC, Yang Z. Microstructure and mechanical properties of 18Mn3Si2CrMo steel subjected to austempering at different temperatures below Ms. *Mater Sci Eng A*. 2018;724:103–11.
19. Plumtree A, Abdel-Raouf HA. Cyclic stress–strain response and substructure. *Int J Fat*. 2001;23:799–805.
20. ASTM E606. Standard Test Method for Strain-Controlled Fatigue Testing. Standard Test Method for Strain-Controlled Fatigue Testing. (2021).
21. Liu D, Bai B, Fang H, Zhang W, Gu J, Chang K. Effect of tempering temperature and carbide free bainite on the mechanical characteristics of a high strength low alloy steel. *Mater Sci Eng A*. 2004;371:40–4.
22. Hilditch T, Beladi H, Hodgson P, Stanford N. Role of microstructure in the low cycle fatigue of multi-phase steels. *Mater. Sci Eng A*. 2012;534:288–96.
23. Ellyin F. *Fatigue Damage, Crack Growth and Life Prediction*, 1st ed. Chapman & Hall: London; 1997. ISBN 0-412-59600-8.
24. Ramberg W, Osgood WR. Description of stress-strain curves by three parameters. NACA TN 902 (1943) National Advisory Committee for Aeronautics.
25. Masing G. Eigenspannungen und verfestigung beim messing. In: *Proceedings of the 2nd International Congress of Applied Mechanics*. Zurich: Orell Fussli Verlag; 1926. p. 332–5.
26. Bai FM, Zhou HW, Liu XH, Song M, Yi Y-X, Huang Z-Y. Masing behavior and microstructural change of quenched and tempered high-strength steel under low cycle. *Fatigue Acta Metall Sin*. 2019;32:1346–54.
27. Xia S, Zhang FC, Yang Z. Cyclic deformation behaviours of 18Mn3Si2CrNiMo multiphase (martensite/bainite/retained austenite) steel. *Mater Sci Eng A*. 2019;74:64–73.
28. Basquin OH. The exponential law of endurance tests. *Am Soc Test Mater ASTM*. 1910;10:625–30.
29. Coffin LF. A study effects of cyclic thermal stresses on ductile metal. *Trans ASME*. 1954;76:931–50.
30. Manson SS. Behaviour of materials under conditions of thermal stress. NACA TN-2933 (1954) National Advisory Committee for Aeronautics.
31. Lesiuk G, Szata M, Rozumek D, Marciniak Z, Correia J, Jesus A. Energy response of S355 and 41Cr4 steel during fatigue crack growth process. *J Strain Anal Eng Des*. 2018;53:663–75.
32. Zhu S-P, Liu Y, Liu Q, Yu Z-Y. Strain energy gradient-based LCF life prediction of turbine discs using critical distance concept. *Int J Fat*. 2018;113:33–42.
33. Smith R, Watson P, Topper T. A stress-strain parameter for the fatigue of metals. *J Mater*. 1970;5:767–78.
34. Liu K. A method based on virtual strain-energy parameters for multiaxial fatigue life prediction. In McDowell D, Ellis J, editors. *Advances in Multiaxial Fatigue*, 1st ed. ASTM International: West Conshohocken; 1993. p. 67–84.

Publisher's Note Springer Nature remains neutral with regard to jurisdictional claims in published maps and institutional affiliations.